Journal of Crystal Growth 310 (2008) 4226–4232

Contents lists available at ScienceDirect

Journal of Crystal Growth

journal homepage: www.elsevier.com/locate/jcrysgro

SnO_2 nanobelts and nanocrystals: Synthesis, characterization and optical properties

Y. Li [a,*], Y.H. Zhao [a], Z.H. Zhang [a], W. Liu [a], V. Ortalan [a], Y.Z. Zhou [a], X.L. Ma [b], E.J. Lavernia [a]

[a] Department of Chemical Engineering and Materials Science, University of California, One Shields Avenue, Davis, CA 95616, USA
[b] Shenyang National Laboratory for Materials Science, Institute of Metal Research, Chinese Academy of Sciences, Shenyang 110016, PR China

ARTICLE INFO

Article history:
Received 4 March 2008
Received in revised form
18 June 2008
Accepted 18 June 2008
Communicated by B.A. Korgel
Available online 24 June 2008

PACS:
62.23.Hj
68.37.Ma
68.37.Og

Keywords:
A1. Characterization
A1. Low dimensional structures
A1. Nanostructures
B1. Nanomaterials
B2. Semiconducting materials

ABSTRACT

SnO_2 nanobelts and nanocrystals have been synthesized in large quantity using the thermal evaporation and oxidation method via careful control of experimental parameters. The products were characterized with scanning electron microscopy, X-ray powder diffraction, transmission electron microscopy, and ultraviolet absorption spectroscopy. The as-synthesized SnO_2 nanobelts primarily consist of tetragonal rutile structure and orthorhombic phases, whereas the composition of the SnO_2 nanocrystals is a relative pure rutile structure. Detailed microstructure characterization reveals that stacking faults and a layered structure exist in the nanobelts and a twin structure was frequently observed in the nanocrystals. The ultraviolet absorption spectra of these two nanostructures were measured. Based on the above microstructural and optical results, the possible growth mechanism, and the structure–properties relationship were discussed for the nanobelts and nanocrystals.

1. Introduction

During recent decades, nanostructured materials have received considerable attention from the scientific and engineering communities [1,2]. These structures exhibit distinct properties from those of bulk materials due to their small size and large surface-to-volume ratios, and accordingly, nanostructured materials have emerged as promising candidates for realizing nanoscale electronic, optical, and mechanical devices with enhanced performance. Among them, one-dimensional (1D) nanomaterials, such as nanowires, nanotubes, and nanobelts can function as both nanoscale device elements and interconnects while keeping unique properties due to size confinement in the radial direction [3,4]. Therefore, 1D nanostructures, in particular semiconductor 1D nanostructures, have been successfully synthesized by various methods such as thermal evaporation [5–7], chemical vapor deposition (CVD) [8,9], laser ablation [10], template [11], and sol–gel [12] techniques. Their optical, electronic, and magnetic properties as well as their potential use in various applications have also been extensively investigated.

Nanocrystals emerged earlier than 1D nanostructures, partly due to the fact that they are readily generated via various experimental methods. These manufacturing methods include: melt crystallization, CVD, laser, self-propagating high-temperature synthesis (SHS), hydrothermal processes and others [13–15]. Nanocrystals have wide application in the electronic, optical, mechanical, magnetic, and sensing materials fields [16,17].

SnO_2, an n-type wide band gap ($E_g = 3.6\,eV$, at $300\,K$) semiconductor with appreciable degree of iconicity, is attractive for potential applications in gas sensors [18,19], catalyst supports [20], and transparent conducting electrodes [21]. Recently, a series of SnO_2 nanobelts, nanowires and nanocrystals have been synthesized and investigated [22–25]. However, systematic comparisons and investigations of the relationship between microstructures and properties of the above different morphologies are still lacking. In this contribution, SnO_2 nanobelts and nanocrystals are synthesized via careful control of the air flow rates of thermal evaporation and oxidation. In addition, their microstructures and optical properties are determined and analyzed. Via comparisons of the microstructures and optical

---

* Corresponding author. Tel.: +1 530 752 9568.
E-mail address: yngli@ucdavis.edu (Y. Li).

0022-0248/$ - see front matter © 2008 Elsevier B.V. All rights reserved.
doi:10.1016/j.jcrysgro.2008.06.046

properties of these two morphologies, our objective is to shed light on the microstructure–properties relationship in nanomaterials.

2. Experiments

A horizontal alumina tube (outer diameter: 8.1 cm; inner diameter: 7.1 cm; length: 98 cm) was mounted inside a high-temperature tube furnace. Powders of metal tin were placed in an alumina crucible. After transferring the crucible to the center of the alumina tube, the tube was evacuated by a mechanical rotary pump to pressure of 10 Pa. During the experiment, a constant flow of Ar mixed with air was maintained at a stable flow rate and the pump continually evacuated the system so that the pressure inside the tube was kept at 5×10^4 Pa. The flow rates used were 100 sccm Ar and 20 sccm air for the preparation of nanobelts, and 100 sccm Ar and 200 sccm air for nanocrystals. Silicon substrates were placed in a position downstream from the air flow in the furnace to collect the reaction products. The temperature of the alumina tube was slowly increased from room temperature to 1150 °C and held at this temperature for 1 h before furnace cooling back to room temperature. After the furnace was cooled down, it was found that a white, wool-like product was suspended from the inner wall of the tube in the case of the nanobelt experiments, and a bright white layer formed on the silicon substrate in the case of the nanocrystal experiments.

Powder X-ray diffraction (XRD) patterns of the products were obtained with an X-ray diffractometer (Bruker D8 with CuKα radiation). Scanning electron microscope (SEM) images were taken on a Philips XL 30 FEG SEM. Transmission electron microscopy (TEM) samples were prepared by dispersing the powder products in alcohol by ultrasonic treatment, dropping them onto a porous carbon film supported on a copper grid, and then drying them in air. Low-magnification images and selected area electron diffraction (SAED) of the as-deposited products were taken on a JEOL-2010 transmission electron microscope. A Tecnai G^2 F30 transmission electron microscope, equipped with high-angle-angular-dark-field (HAADF) detector, Gatan imaging-filter (GIF) energy dispersive X-ray spectroscopy (EDX) systems, was used for Z-contrast imaging and composition analysis. A UV–vis spectrophotometer (JASO-V550) was used to obtain the optical absorbance spectra of the samples.

3. Results and discussion

3.1. Microstructures

Fig. 1(a) and (b) is the SEM image of the as-synthesized products, the morphology and scale of the nanobelts and nanocrystals are clearly evident. It is confirmed from a number of SEM images that the length of the nanobelts ranges from several tens of micrometers to the order of millimeters. The width of the nanobelts is about 100–200 nm, while the diameter of nanocrystals is about 30–50 nm. Moreover, it is discernable that both of the products are present in large quantities.

XRD patterns reveal the composition and crystal structure of the as-synthesized products, as shown in Fig. 2(a). The majority of the diffraction peaks for nanobelts can be indexed to the tetragonal rutile SnO_2 (space group number 136) with lattice parameter of $a = 4.72$ Å and $c = 3.19$ Å (JCPDS 41-1445). Some of the peaks are indexed to the orthorhombic phase SnO_2, which implies that some nanobelts consist of orthorhombic SnO_2 (space group number 19) with lattice parameter of $a = 4.714$ Å, $b = 5.727$ Å, and $c = 5.214$ Å (JCPDS 29-1484). In addition, some

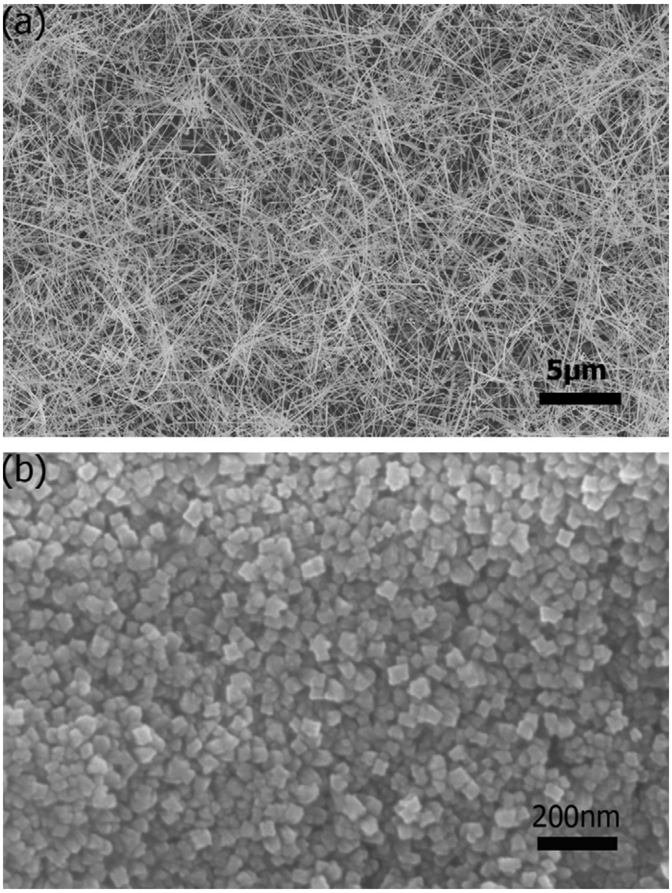

Fig. 1. (a) SEM image showing the typical morphologies of the as-synthesized SnO_2 nanobelts and (b) SEM image showing the typical morphologies of nanocrystals.

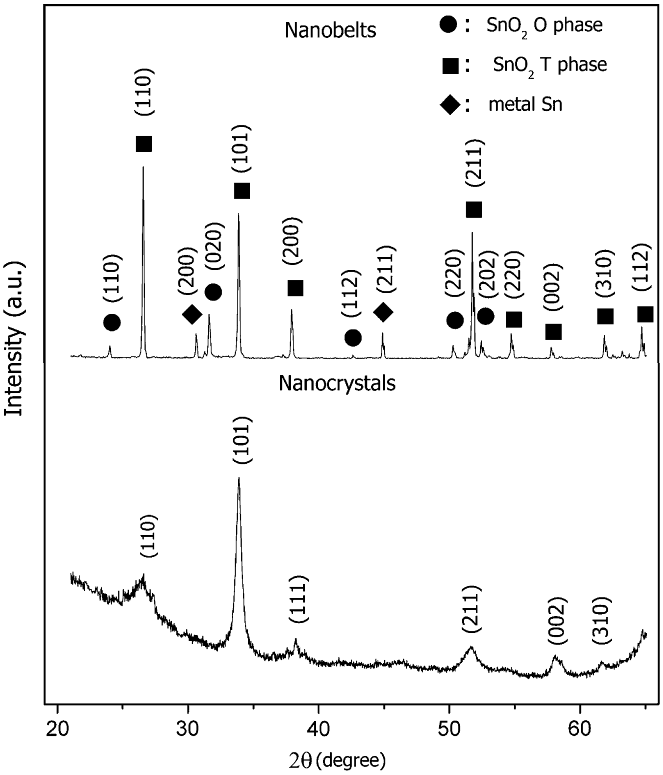

Fig. 2. XRD pattern of the as-synthesized nanobelts and nanocrystals.

metallic Sn peaks were also found that result from residual starting materials. The lower XRD pattern in Fig. 2(b) is from nanocrystals, supporting the argument that rutile SnO_2 is the main composition of the nanocrystals. The increased background intensity at both ends of the XRD pattern originates from the Si substrate. Compared with the results of the nanobelts, an evident peak broadening exists in the XRD patterns of nanocrystals due to the small crystal size (as revealed by SEM). It is interesting that there is no obvious peak broadening for nanobelts though their radial size is in the sub-micrometer range. The sharp XRD peak of the nanobelts can be attributed to their relatively large length (up to several millimeters).

Fig. 3(a) is a low-magnification HAADF image of nanobelts showing details of the typical morphology; the cross-section of a nanobelt marked by an arrowhead can be seen. It indicates that the widths of the nanobelts are 4–5 times larger than those of the thickness dimension. The EDX composition analysis also was conducted for the thin nanobelts. Fig. 3(b) is the EDX results with TEM of which the characteristic spectrum reveals the composition included Sn and O elements. Quantitative analysis reveals the atomic ratio of Sn and O as 35:65 that is consistent with atomic ratio in the SnO_2. The Cu peak comes from the microgrid and carbon film used to support the TEM sample. Fig. 4(a) is a bright field TEM image of several nanobelts, the marked curved nanobelt provides experimental support to the suggestion that the products consist of belt-like nanostructures. Fig. 4(b) is an enlarged TEM image of a nanobelt, and Figs. 4(c) and (d) are corresponding to SAED patterns and high-resolution electron microscopy (HREM) image, respectively. It is seen that the growth direction of the belt

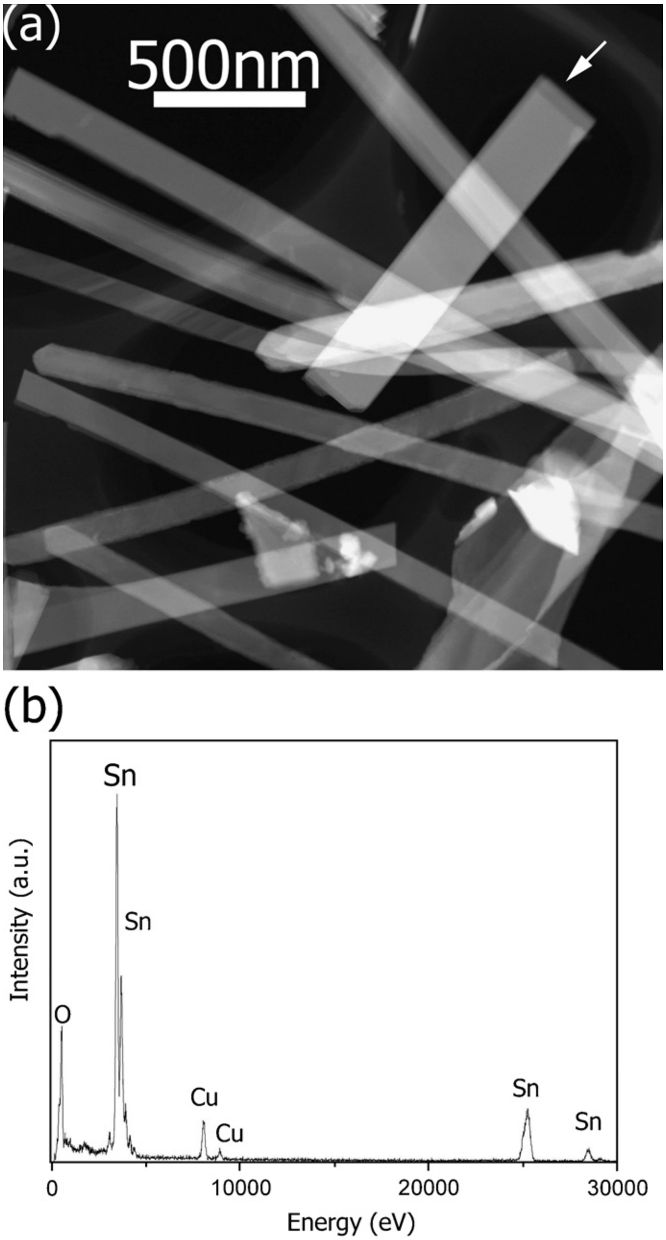

Fig. 3. (a) Low-magnification HAADF image of SnO_2 nanobelts and (b) corresponding EDX results showing the composition of nanobelts.

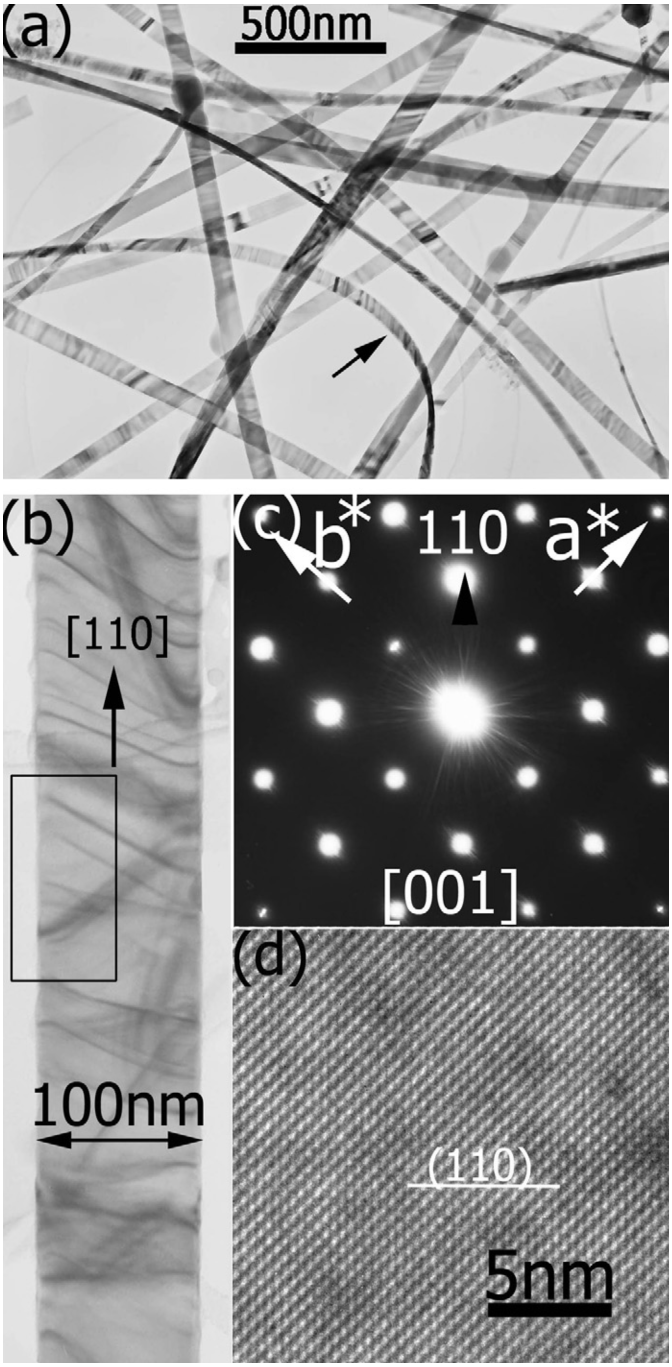

Fig. 4. (a) TEM image of several nanobelts, curved one of them was marked to verify the belt-like structure, (b) TEM image of one tetragonal SnO_2 nanobelts, (c) corresponding SAED patterns, and (d) HREM image.

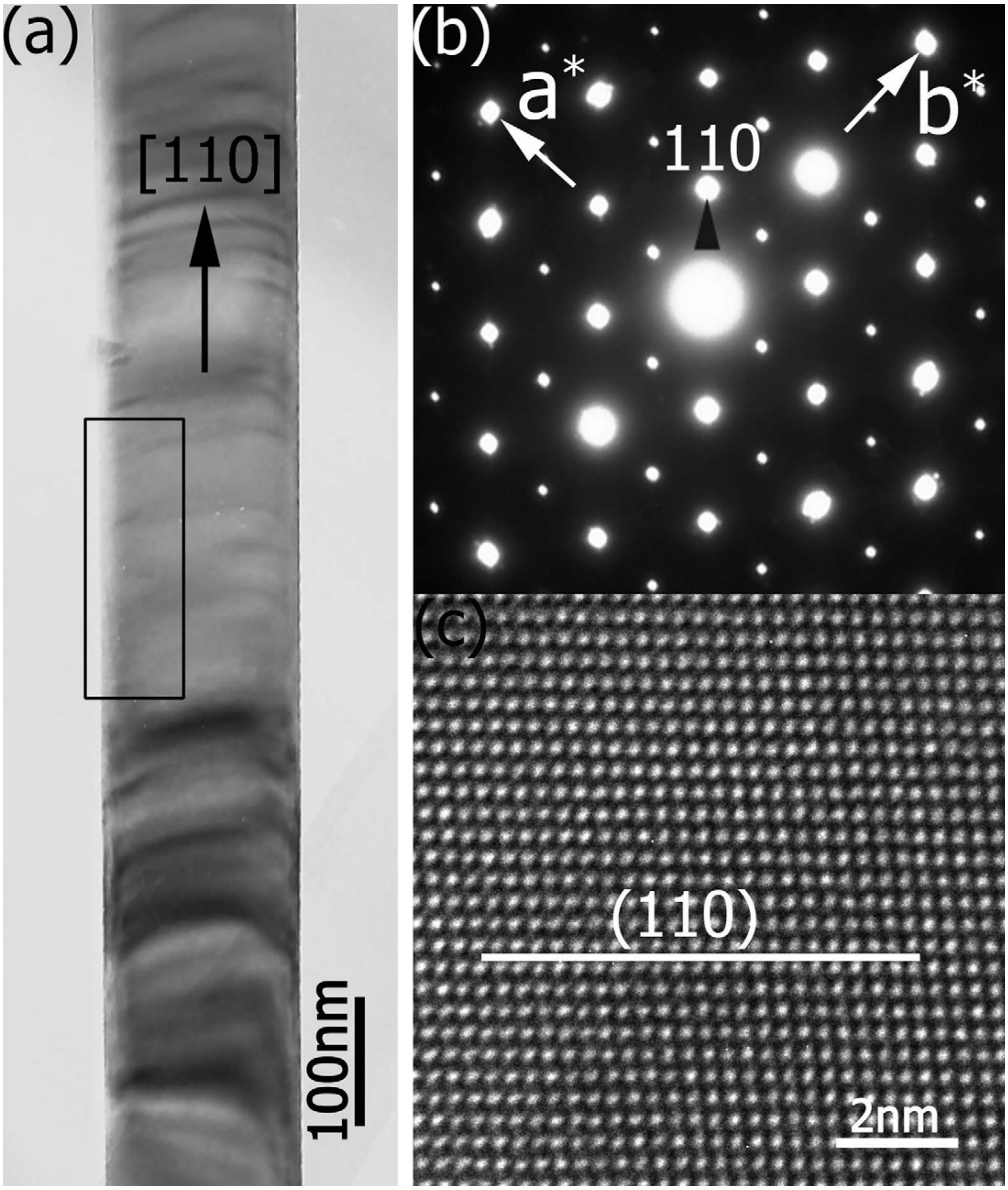

Fig. 5. (a) TEM image of one orthorhombic SnO_2 nanobelt, (b) corresponding SAED patterns, and (c) HREM image.

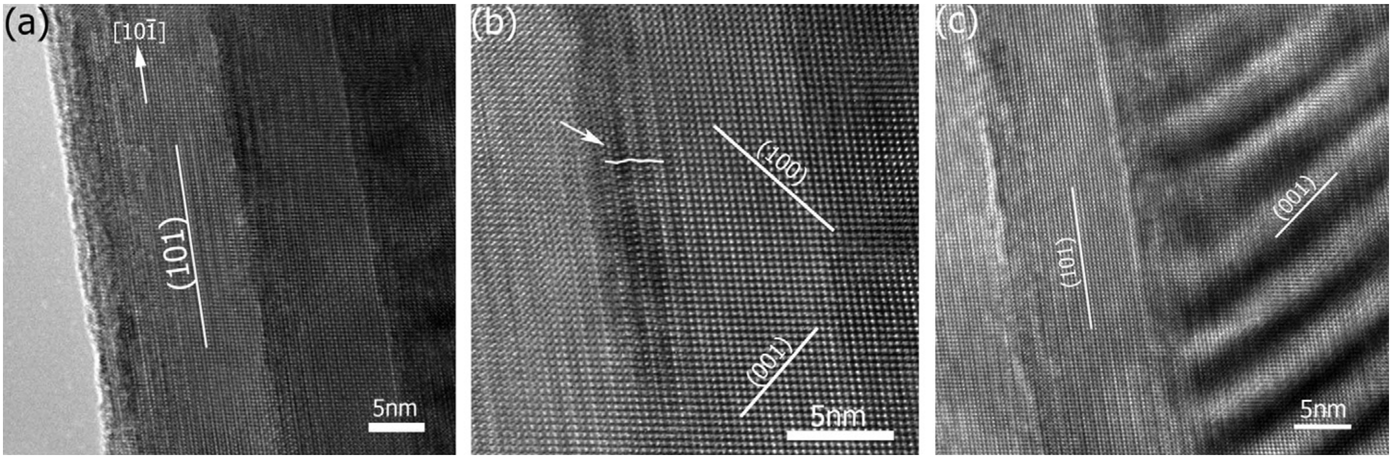

Fig. 6. (a) HREM image of edge of an orthorhombic SnO_2 nanobelt showing the step structure, (b) partial HREM image of a nanobelt showing the existence of stacking faults, and (c) partial HREM image from the step structure showing a lot of Moiré patterns.

is along [1 1 0]. In addition, the calculated lattice parameter *a* value from SAED patterns is 4.74 Å, consistent with XRD results.

In addition to the rutile SnO_2 nanobelts, detailed TEM studies also revealed nanobelts with an orthorhombic structure. Fig. 5(a) is the TEM image obtained from orthorhombic nanobelts, while Fig. 5(b) and (c) are the corresponding electron diffraction pattern and high-resolution images, respectively. The main growth direction of the orthorhombic SnO_2 nanobelts is also [1 1 0], and some nanobelts growing along $[1\,0\,\bar{1}]$ were also observed. Fig. 6(a) presents HREM image of the edge orthorhombic SnO_2 nanobelt growing along $[1\,0\,\bar{1}]$, two obvious step structures along the (1 0 1) plane can be clearly detected therein. This observation implies that the growth mode of orthorhombic SnO_2 nanobelts can be described as a layer-by-layer growth mode, similar to the case of tetragonal SnO_2 nanobelts, as previously reported [24]. Some stacking faults are found to exist in the nanobelts, where the stacking faults structure along (1 0 1) planes are marked by an arrow, as shown in Fig. 6(b). Small differences were observed between the step structures reported here and those observed in previous work, many equal width Moiré patterns were found in a layer of the nanobelts (Fig. 6(c)). Generally, the Moiré fringes result from the overlap of two different crystals plane or from same crystal plane that contains some misorientation. It is apparent that in our case the presence of Moiré fringes

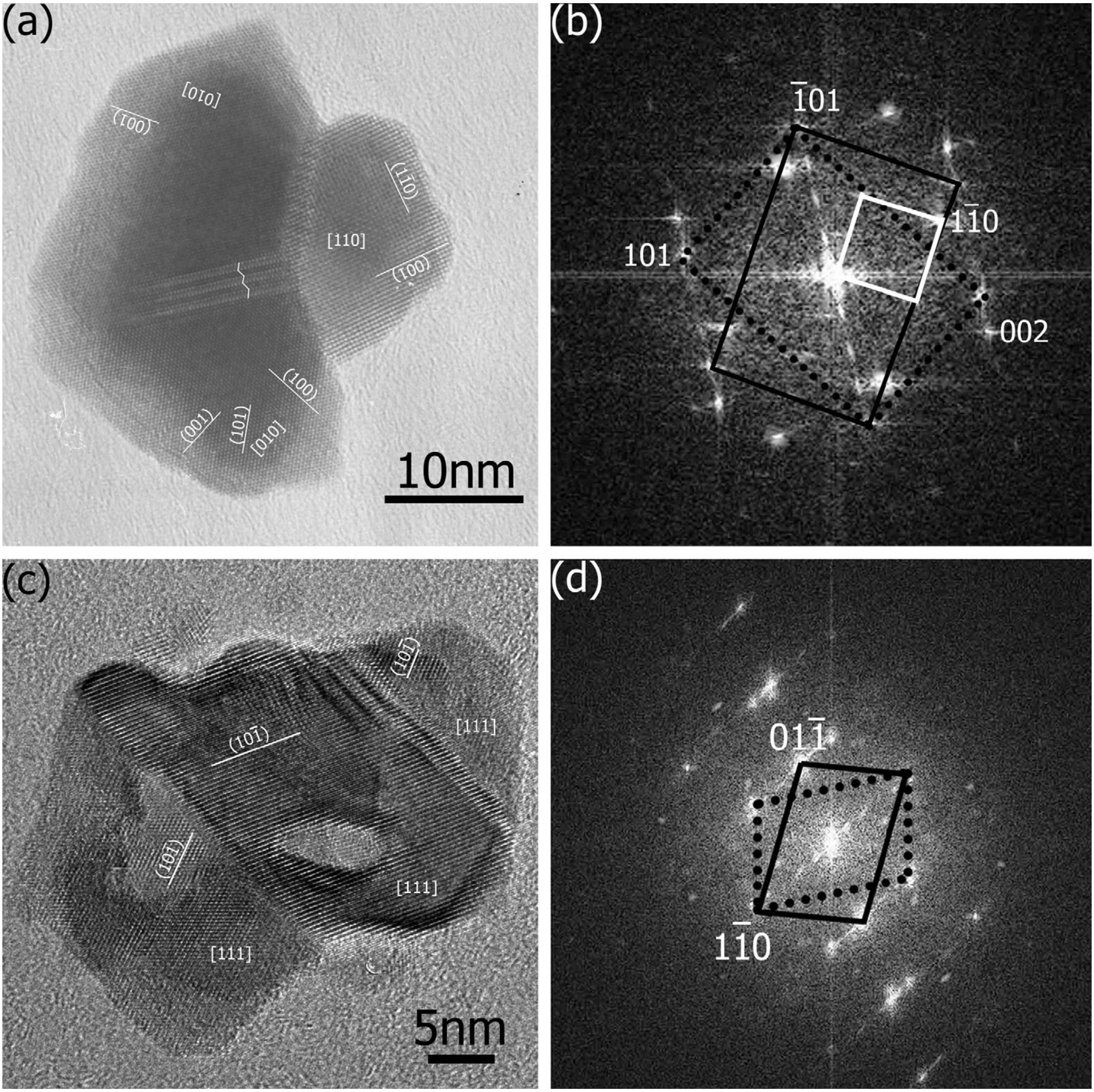

Fig. 7. (a) HREM image of a typical nanocrystal indicates that it consists of three parts, (b) the corresponding FFT pattern of (a), (c) HREM image of another typical nanocrystal, and (d) the corresponding FFT pattern of (c).

can be attributed to the overlap of two layers with some misorientation.

In comparison with the nanobelts, the nanocrystals have more lattice defects. A typical HRTEM image of a nanocrystal is shown in Fig. 7(a), and shows that two SnO_2 sections with $[010]$ zones are separated by a group of $(10\bar{1})$ staking faults and symmetrically form $(10\bar{1})$ twins, the other SnO_2 section is with $[110]$ zone axis. Fig. 7(b) is the corresponding fast fourier transformation (FFT) pattern, in which the twins relationships are depicted by two rectangles consisting of diffraction spots from the twins and matrices. The diffraction spots are also illustrated by a white rectangle. Fig. 7(c) is a TEM image for another typical nanocrystal, which includes three sections that are separated by two parallel (110) twins planes. The corresponding twin relationship is also depicted in the FFT patterns in Fig. 7(d).

According to the classical growth mechanism [26], the growth of our SnO_2 nanobelts cannot be attributed to a vapor–liquid–solid process, in which the morphology feature is a catalyst particle located at the end of the nanowire or nanobelts. In fact, no nanoparticle was observed on the tips of the nanobelts. Therefore, it is likely that the growth mechanism of SnO_2 nanobelts can be ascribed to a vapor–solid (VS) mechanism [5,27]. We propose that during heating, the Sn vapor generated from the Sn powder (with a melting point of 231.9 °C) combines with oxygen, to form SnO vapor (with a melting point of 1080 °C). It is well-known that SnO is metastable and will decompose into SnO_2 and Sn at some certain suitable regions [23,28,29]. The decomposed SnO_2 directly deposited on the walls of the alumina furnace forming SnO_2 seeds. Due to the gradient temperature field, the deposited SnO_2 seeds grow into nanobelts with further deposition of SnO_2 molecular. In related studies, bulk orthorhombic SnO_2 has been synthesized at a high pressure of 158 Kbar, and Dai et al. reported the synthesis of small amount of orthorhombic SnO_2 nanobelts mixed with dominant rutile SnO_2 [22,30], which is similar with the present results. Despite these studies, the formation mechanism responsible for the orthorhombic SnO_2 structure remains unclear. In the case of the formation of the nanocrystals, the oxygen concentration probably plays an important role in the experiment. The higher oxygen concentration might promote a $Sn_{metal} \rightarrow SnO_2$ transformation at a fast rate and produced large amount of SnO_2 clusters (with a melting point of 1630 °C higher than our reaction temperature). The SnO_2 clusters cannot be transported by air flow which probably impedes the growth of SnO_2 nanobelts at the inner wall of alumina. As a result, a large number of SnO_2 clusters accumulate in the Si substrate forming nanocrystals. Additional detailed studies of the relevant growth mechanisms of these two nanoforms are underway.

3.2. Optical properties

The ultraviolet absorption spectra of the SnO_2 nanobelts and nanocrystals at room temperature were measured using a xenon lamp as an excitation source and an excitation wavelength of 325 nm, as shown in Fig. 8. It is clear that the spectrum of the nanobelts consists of a flat and strong absorption peak located at 262.5 nm and that the nanocrystals have a relative sharp peak at 269 nm. The peak position corresponding to the nanocrystals is close to that reported in a prior study, 271 nm [31]. It is apparent that the ultraviolet absorption spectrum of nanocrystals has a red-shift relative to the spectrum from nanobelts. This observation can be attributed to the fact that nanocrystals have more defects structures, such as twins and stacking faults relative to nanobelts. These defect structures have an important effect, in that they limit free electrons that form metastable trap states [32]. The metastable trap effectively reduces the energy of the electrons that are excited from the valence band to the conduction band. Hence one can anticipate an absorption peak with a longer wavelength in the case of nanocrystals as compared to that for nanobelts. In addition, the morphology of the materials may also affect their optical properties due to different specific surface areas, which is being investigated further.

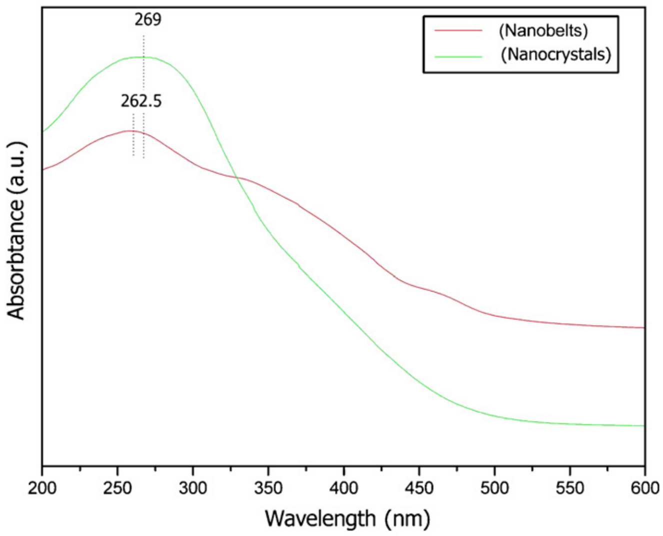

Fig. 8. Ultraviolet absorption spectra of the as-synthesized nanobelts and nanocrystals.

4. Conclusions

Thermal evaporation and oxidation of tin powders at 1150 °C in a high-temperature tube furnace was used to successfully synthesize tetragonal and orthorhombic SnO_2 nanobelts and nanocrystals. SEM, XRD, EDX, SAED, and HREM were used for phase identification and microstructure characterization in these nanostructures. The lengths of the nanobelts were up to several millimeters and the typical width and thickness were in the ranges of 30–150 and 10–30 nm, respectively. The average size of the nanocrystals is 30–50 nm. Detailed microstructure characterization reveals that stacking faults and a layer structure were present in the nanobelts and twin structures were frequently found in the nanocrystals. Analysis indicates that oxygen concentration may play a key role in the formation of nanobelts and nanocrystals during the synthesis experiments. The characteristic ultraviolet absorption spectra of these two nanostructures were also measured. The higher concentration of defects in the nanocrystals is thought to be responsible for the observed differences in optical properties.

Acknowledgments

The authors (YL, YHZ, ZHZ, WL, YZZ, and EJL) would like to acknowledge the financial support from the Office of Naval Research under Grant no. N00014-04-1-0370. XLM would like to thank the financial support from the National Outstanding Young Scientist Foundation of China under Grant no. 50325101 and the Special Funds for the Major State Basic Research Projects of China (Grant no. 2002CB613503). The authors would also like to thank Doctor G. Liu for the help to measure the ultraviolet absorption spectra.

References

[1] C.R. Martin, Science 266 (1994) 1961.
[2] H.J. Dai, E.W. Wong, C.M. Lieber, Science 272 (1996) 523.
[3] P.D. Yang, H.Q. Yan, S. Mao, R. Russo, J. Johnson, R. Saykally, Adv. Funct. Mater. 12 (2002) 323.

[4] M.H. Huang, S. Mao, H. Feick, H.Q. Yan, Y. Wu, H. Kind, Science 292 (2002) 1897.
[5] Z.W. Pan, Z.R. Dai, Z.L. Wang, Science 291 (2001) 1947.
[6] J.S. Lee, S.K. Sim, B. Min, K. Cho, S.W. Kim, S. Kim, J. Crystal Growth 267 (2004) 145.
[7] Y. Li, L.H. Qian, W.F. Li, C.N. Yang, X.L. Ma, Appl. Phys. Lett. 87 (2005) 183107.
[8] T.I. Kamins, R.S. Williams, D.P. Basile, J. Appl. Phys. 89 (2001) 1008.
[9] Y. Li, X.L. Ma, Phys. Status Solidi A 202 (2005) 435.
[10] A.M. Morales, C.M. Lieber, Science 279 (1998) 208.
[11] W. Wang, N. Li, X.T. Li, W.C. Geng, S.L. Qiu, Mater. Res. Bull. 41 (2006) 1417.
[12] Y. Lei, L.D. Zhang, G.W. Meng, G.H. Li, X.Y. Zhang, C.H. Liang, W. Chen, S.X. Wang, Appl. Phys. Lett. 78 (2001) 1125.
[13] A. Nakajima, Y. Sugita, K. Kawamura, H. Tomita, N. Yokoyama, J. Appl. Phys. 80 (1996) 4006.
[14] P. Moriarty, Rep. Prog. Phys. 64 (2001) 297.
[15] M.M. Wu, G. Lin, D.H. Chen, G.G. Wang, D. He, S.H. Feng, R.R. Xu, Chem. Mater. 14 (2002) 1974.
[16] Z.T. Liu, C. Lee, V. Narayanan, G. Pei, E.C. Kan, IEEE Trans. Electron Devices 49 (2002) 1606.
[17] M. Bruchez, M. Moronne, P. Gin, S. Weiss, A.P. Alivisatos, Science 281 (1998) 2013.
[18] J.S. Suehle, R.E. Cavicchi, M. Gaitan, S. Semancik, IEEE Electron Device Lett. 14 (1993) 118.
[19] E. Comini, G. Faglia, G. Sberveglieri, Z.W. Pan, Z.L. Wang, Appl. Phys. Lett. 81 (2002) 1869.
[20] W. Dazhi, W. Shulin, C. Jun, Z. Suyuan, L. Fangqing, Phys. Rev. B 49 (1994) 282.
[21] Y.S. He, J.C. Campbell, R.C. Murphy, M.F. Arendt, J.S. Swinnea, J. Mater. Res. 8 (1993) 3131.
[22] Z.R. Dai, J.L. Gole, J.D. Stout, Z.L. Wang, J. Phys. Chem. B 106 (2002) 1274.
[23] J.Q. Hu, X.L. Ma, N.G. Shang, Z.Y. Xie, N.B. Wang, C.S. Lee, S.T. Lee, J. Phys. Chem. B 106 (2002) 3823.
[24] X.L. Ma, Y. Li, Y.L. Zhu, Chem. Phys. Lett. 376 (2003) 794.
[25] Y.J. Chen, Q.H. Li, Y.X. Liang, T.H. Wang, Q. Zhao, D.P. Yu, Appl. Phys. Lett. 85 (2004) 5682.
[26] Y.N. Xia, P.D. Yang, Y.G. Sun, Y.Y. Wu, B. Mayers, B. Gates, Y.D. Yin, F. Kim, H.Q. Yan, Adv. Mater. 15 (2003) 353.
[27] P.D. Yang, C.M. Lieber, J. Mater. Res. 12 (1997) 2891.
[28] D.W. Yuan, R.F. Yan, G. Simkovich, J. Mater. Sci. 34 (1999) 2911.
[29] J.C. Nover, F.D. Richardson, Trans. Inst. Min. Metall. 81 (1972) c63.
[30] K. Suito, N. Kawai, Mater. Res. Bull. 10 (1975) 677.
[31] J.Y. Kang, S. Tsunekawa, A. Kasuya, Appl. Surf. Sci. 174 (2001) 306.
[32] Catherine J. Murphy, Anal. Chem. 521A (2002).